Supplemental Information: Step-induced double-row pattern of interfacial water on rutile TiO_2(110) at electrochemical conditions

Yan Sun[1], Cheng-Rong Wu[1], Feng Wang[1], Rui-Hao Bi[1], Yong-Bin Zhuang[1], Shuai Liu[1], Ming-Shu Chen[1], Kelvin H.-L. Zhang[1,2,*], Jia-Wei Yan[1,*], Bing-Wei Mao[1], Zhong-Qun Tian[1,2], and Jun Cheng[1,2,*]

[1]State Key Laboratory of Physical Chemistry of Solid Surfaces, iChEM, College of Chemistry and Chemical Engineering, Xiamen University, Xiamen 361005, China
[2]Innovation Laboratory for Sciences and Technologies of Energy Materials of Fujian Province (IKKEM), Xiamen, China
[*]chengjun@xmu.edu.cn; jwyan@xmu.edu.cn; kelvinzhang@xmu.edu.cn

Preparation of rutile TiO_2 (110) surface

The samples we used were 0.5 wt% Nb doped rutile TiO_2 (110) oriented single crystal (Crystec GmbH), which underwent chemical etching and annealing treatment to obtain atomically flat surfaces with $[1\bar{1}1]$ steps. The samples were treated by HF etching in buffered oxide etchant (BOE, NH_4F : HF = 10 : 1) and then annealed at 950 °C in the oxygen flow to obtain atomically smooth surfaces. Atomic force microscope (AFM) was performed by NanoWizard (JPK instruments).

Cyclic voltammetry

The electrochemical experiments were carried out on a single-chamber electrochemical cell. An AUTOLAB workstation (EcoChimie, Netherlands) equipped with fast scan SCAN250 module was used, and cyclic voltammetry was performed in linear mode optimized for fast process measurements. The electrolyte was 0.1 M perchloric acid solution prepared by perchloric acid (Merck, Suprapur) and ultra-pure water (18.2 $M\Omega \cdot cm$, Milli-Q), and the working electrode was rutile TiO_2 (110) single crystal. Prior to each experiment, the reference electrode silver wire and counter electrode platinum wire were boiled in ultra-pure water (18.2 $M\Omega \cdot cm$, Milli-Q) for at least three times for cleaning and stabilizing. After experiments, the reference electrode was immediately calibrated to Saturated Calomel Electrode (SCE).

EC-STM setup

In-situ STM measurements were carried out on a Multimode VIII STM instrument (Bruker, Santa Barbara, CA) under constant current mode. The EC-STM tips, mechanically cut from a Pt/Ir wire (Pt80/Ir20; ϕ=0.25 mm), were insulated by thermosetting polyethylene to reduce Faradaic current, and they were stable in the potential window studied (see Figure S2 in SI). In the EC-STM cell, the working electrode was rutile TiO_2 (110) single crystal freshly prepared before each experiment, and the counter electrode was Pt wire. The electrolyte is 0.1 M $HClO_4$, prepared by perchloric acid (Merck, Suprapur) and ultra-pure water (18.2 $M\Omega \cdot cm$, Milli-Q). The reference electrode used was Pt quasi-reference electrode. STM images are obtained under constant potential (cell current density is -0.35 $\mu A/cm^2$ when the sample potential is -0.38 V). All experiments are carried out under N_2 atmosphere. The constant scan rate conducted in EC-STM was 30 Hz with 256 points per line for magnified images, corresponding to about 0.1 ms per image pixel, and for large area EC-STM images, the constant scan rate was 4 Hz.

Height of step on rutile TiO_2(110)

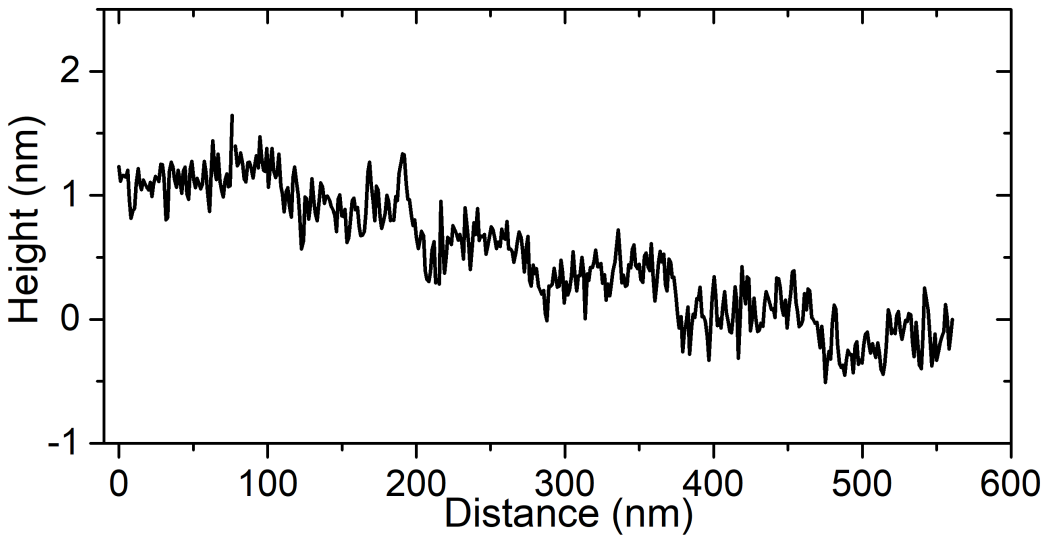

Figure S1. Vertical profile along the direction perpendicular to the steps on rutile TiO_2(110) in the atomic force microscopy image of Figure 1b. The measured step height is 3.2±0.5Å.

Tip potential

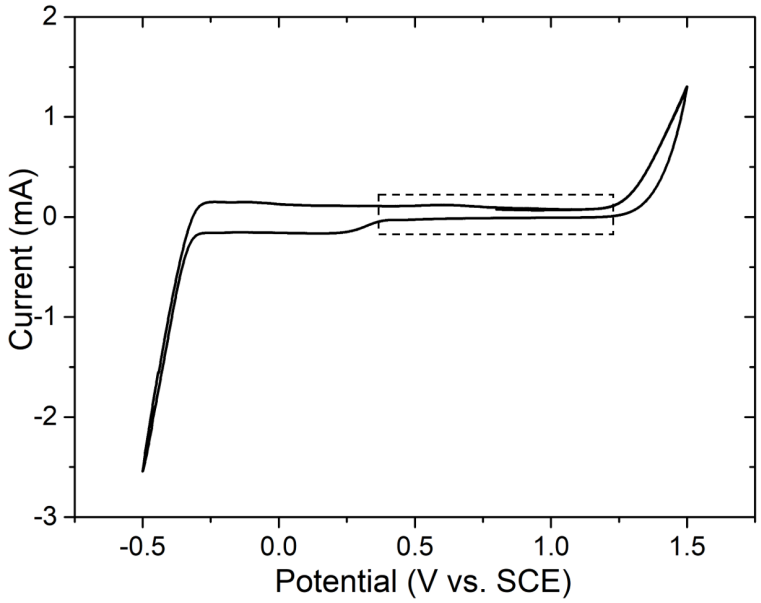

Figure S2. Cyclic voltammogram of Pt/Ir wire in 0.1 M $HClO_4$. The counter electrode is platinum wire with saturated calomel electrode (SCE) as reference. The scan rate is 1 V s^{-1}. The dashed rectangle indicates the potential range of the Pt/Ir tip for the STM imaging.

Sample potential

To determine the optimal sample potential (E_{sample}) for electrochemical scanning tunneling microscope (EC-STM) images, we tested sample potential from -0.18 V (onset potential of reduction reaction in CV in Figure 2a) to -0.8 V vs SCE. We found that -0.38 V is the optimal potential for obtaining atomic STM images with high quality. When the potential becomes too negative, e.g. -0.8 V, it is difficult to get high resolution images due to hydrogen evolution reaction.

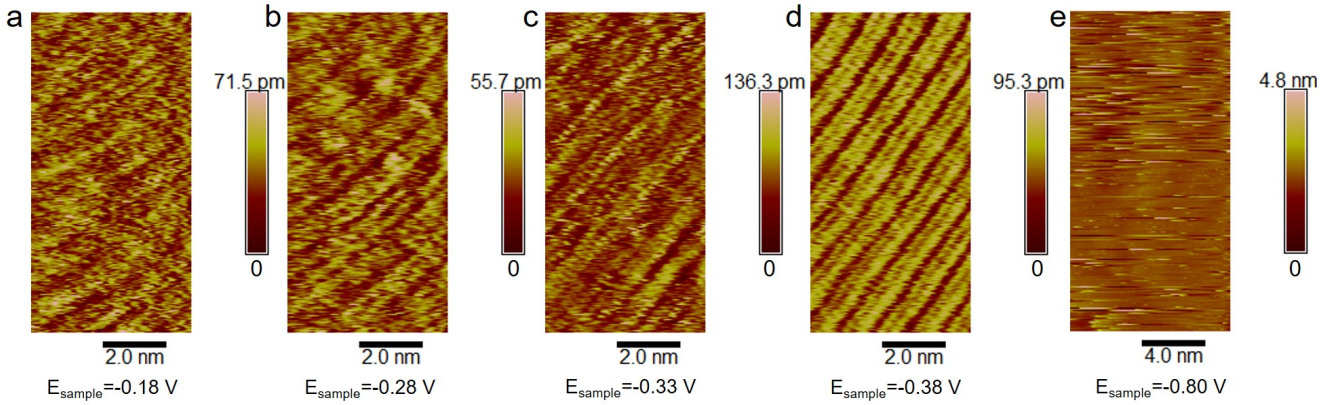

Figure S3. EC-STM images of the rutile TiO_2 (110) in 0.1 M $HClO_4$ with different sample potential: (a) 5×10 nm^2 under E_{sample} = -0.18 V. (b) 5×10 nm^2 under E_{sample} = -0.28 V. (c) 5×10 nm^2 under E_{sample} = -0.33 V. (d) 5×10 nm^2 under E_{sample} = -0.38 V. (e) 10×20 nm^2 under E_{sample} = -0.8 V. All images are under E_{tip} = 1.27 V and I_{tunnel} = 1 nA. All potentials are referenced to SCE.

Reproducibility of EC-STM images

In order to rule out experimental uncertainties, such as noise and double tip, we have repeated EC-STM many times and reproduced the same double-row feature in high resolution EC-STM images with different tips on different dates. For example, Figure 2d in main text was carried on 17^{th} 2021, the inset of Figure 2d was on 10^{th} March 2021, Figure S4a was on 11^{th} March 2021 and Figure S4b was on 5^{th} March 2021. In every experiment, the single crystal surface was re-etched and annealed, or even replaced by a new single crystal, and a freshly made STM tip was always used. It is worth noting that in all obtained images the angle between bright lines and the direction of steps is the same, and very close to the angle between the $[1\,\bar{1}\,1]$ and [001] direction on TiO_2(110) surface. And the spacing of double-row has good repeatability, which can rule out the effect of double tip.

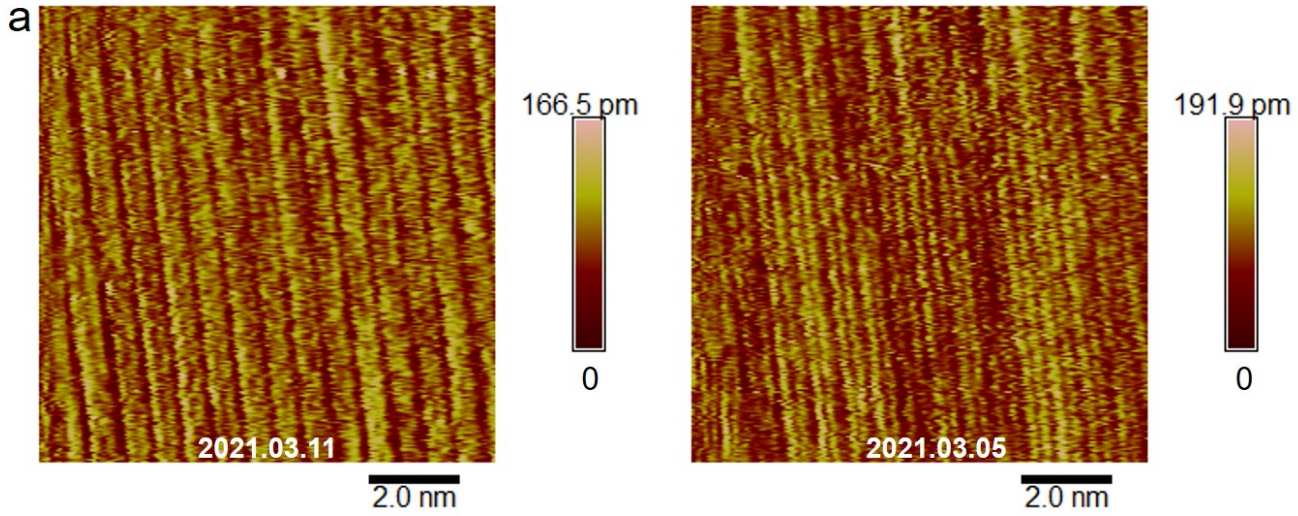

Figure S4. 10×10 nm^2 EC-STM images of the rutile TiO_2 (110) in 0.1 M $HClO_4$ with different tips in different experiments. All images are obtained under E_{sample}=-0.38 V vs. SCE, E_{tip}=1.27 V vs. SCE and I_{tunnel}=1 nA

Preparation of slab models with $[1\,\bar{1}\,1]$ step

In the EC-STM image, we observed a double row pattern running against the $[1\bar{1}1]$ step. To test our hypothesis that the double row pattern is induced by $[1\bar{1}1]$ step edge using MLMD simulation, the first crucial step is constructing a representative atomic model. Surface science studies have uncovered that TiO_2 $(1\,1\,0)$ surface has well-defined steps, where the step edges run parallel to direction [001] and $[1\bar{1}1]$, predominantly[1]. In proposing atomic configurations for these step edges, Diebold et al. have suggested cutting the upper terrace using the concept of autocompensation and charge-neutrality.[1] That means removing same amount of Ti→O and O←Ti from the upper terrace. Later, in the simulation community, Martinez et al. [2] and Hardcastle et al. [3] have constructed symmetric slabs by cutting bulk TiO_2 using high index surface like $[4\,5\,1]$ or $[5\,6\,1]$ ($[n\ \ n+1\ \ 1]$) to expose the $[1\,\bar{1}\,1]$ step-edge. This slab generation scheme would expose a $Ti_{4c}-Ti_{5c}$ step-edge unit at surface, as well as $n-1$ terminal Ti_{5c} sites on the terrace.

We prepared several slabs with step-edges using techniques described above. Figure S5 shows the side and top views for cutting the edge from bulk TiO_2. The TiO_2 unit cell is taken from crystal database, where $a = 4.593(2)$ Å, and $c = 2.959(2)$ Å. In cutting the slab model, we choose to have 5 Ti−O tri-layers and two Ti_{5c} and O_{br} double-rows. After the slab models were cut from the bulk, water boxes of a height of 25 Å were added between upper and lower surfaces of the slabs to form interface models.

The simulation cell parameters of all interface models are shown in Table S1.

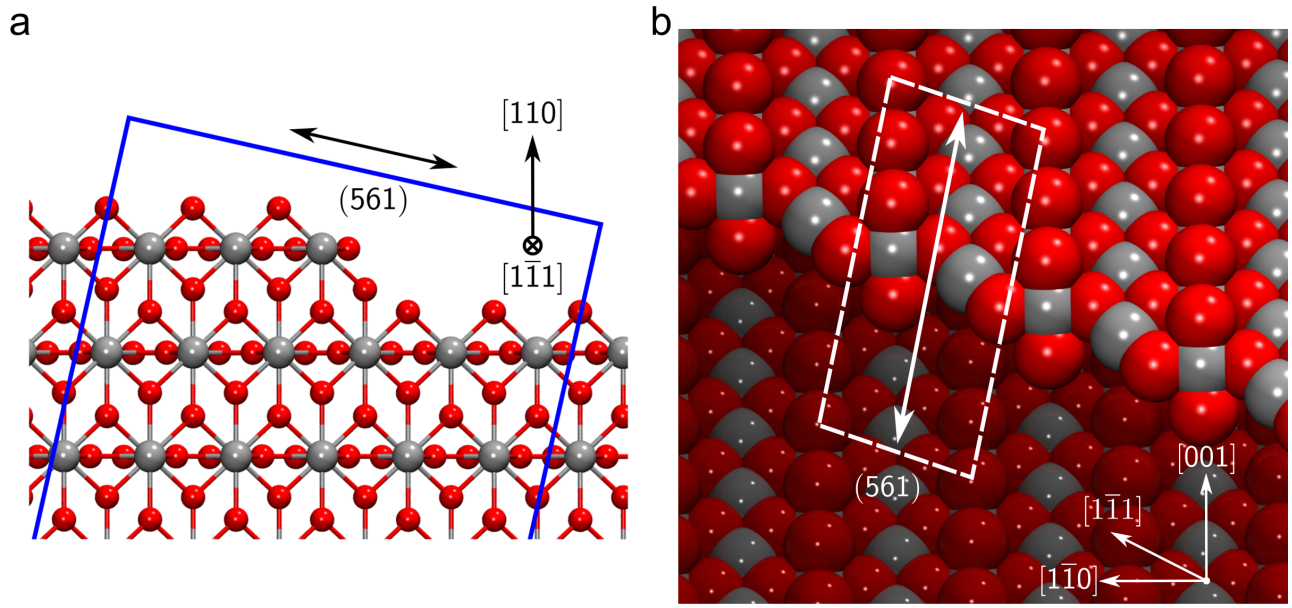

Figure S5. Atomic structures for TiO_2 $[1\,\bar{1}\,1]$ step-edge and high-index surfaces used for cutting the surface. (a) Side view of the step-edge model along $[1\,\bar{1}\,1]$ direction. (b) Top view of the step-edge model.

Table S1. Cell parameters for all interface models used in the simulations.

	a (Å)	b (Å)	c (Å)	α (deg)	β (deg)	γ (deg)	N_{atoms}	Miller index	description
Flat $4\times2\times5$ model	11.84	12.99	38.53	90.0	90.0	90.0	603	$(1\,1\,0)$	Training set
$[1\,\bar{1}\,1]$ edge model #1	15.49	14.28	48.32	90.0	90.0	78.2	1068	$(5\,6\,1)$	Training set
$[1\,\bar{1}\,1]$ edge model #2	15.49	14.28	48.32	90.0	90.0	78.2	1038	$(5\,6\,1)$	Training set
$[1\,\bar{1}\,1]$ edge model #3	27.02	14.28	48.15	90.0	90.0	72.6	1785	$(9\,10\,1)$	MLMD: 8-Ti
$[1\,\bar{1}\,1]$ edge model #4	50.51	14.28	47.84	90.0	90.0	69.3	3240	$(17\,18\,1)$	MLMD: 16-Ti

Training of machine learning potential

Although, classical molecular dynamics (CMD) could already give some insight into the interfacial structure of TiO_2-water interfaces[4], the dissociation of water on the TiO_2 surface needs to be defined manually, which leads to uncertainties in the simulation during the CMD simulation. Therefore, machine learning molecular dynamics (MLMD) is applied to simulate these interfacial structures. Two sets of machine learning potentials (MLP) were fitted in this work; one was for the step-free rutile TiO_2 (110) water interface, and another for the TiO_2 water interface with a $[1\bar{1}1]$ step. The details of simulation supercells are shown in Table S1. The MLP model adapted in this work is Deep Potential-Smooth Edition (DeePMD-SE)[49] , and details of the DeePMD-SE can be found in ref. [5]. In this MLP model, the total energies E of the given structures are decomposed into a sum of atomic energy contributions[26,27], i.e. $E = \sum_i E_i$, where i is the index of the atom and E_i is the atomic energy of atom i. Each atomic energy is fully determined by the position of the ith atom and its local environment. An embedding neural network is applied to construct a one-to-one mapping between the local environments and mathematical descriptors so that the local environments could be used for training MLP. Then, a fitting neural network is used to construct a one-to-one mapping from descriptors to atomic energies and atomic forces. The size of embedding neural network we used was (25, 50, 100) and the fitting neural network was set to (240, 240, 240). The cutoff radius R_c for descriptors of local environments is set to 6 Å and a smooth function is applied so that the components can smoothly decay to zero at the boundary of descriptors. The initial learning rate was set to 1.0×10^{-3} and it decayed to 5×10^{-8} in 1,000,000 training steps. The training errors for these two MLPs were rather small, as shown in Table S2 and Figure S6, indicating the good accuracy of the trained MLPs.

In order to obtain representative DFT data sets for all MLPs, concurrent learning workflow (deep potential generator, DP-GEN)[6, 7] is applied to sample the PES and collect configurations for DFT calculation on-the-fly during the MLP training processes. DP-GEN contains three steps, *training*, *exploration* and *labeling*. To initialize the DP-GEN, about 10 ps AIMD trajectories are generated and 100 configurations are selected as the initial training sets for MLPs. Then, in order to explore the PES and select representative configurations, during the *training* process, four MLPs are trained on the same data sets with different parameters of deep neural network with 200,000 steps. In *exploration*, one of the four MLPs is used to drive MLMD simulation and maximum force deviations (model deviation, σ[7]) among the four MLPs are computed on each structure of MLMD trajectories. 50 to 100 structures with σ in [0.25, 0.40] eV/Å are selected as new configurations and computed with DFT in *labeling* process. By updating the data sets with DFT labeled configurations, the next iteration of DP-GEN starts. The temperatures of MLMD simulations are set to 330, 430 or 530K and the lengths of trajectories are increased from 10 ps to 30 ps with the number of DP-GEN iteration. The DP-GEN iteration stops when the ratio of structures with $\sigma < 0.25$ in exploration is larger than 99% and then data sets are used to train final MLPs. In training MLPs of TiO_2(110) with $[1\bar{1}1]$ step, the initial data sets are selected from the MLMD trajectories generated by MLP of step-free TiO_2(110), and the data sets of step-free TiO_2(110) are also included in initial data sets in order to reduce the iterations of DP-GEN.

Table S2. Number of structures in the DFT data set, the root-mean-square-error (RMSE) of the energies and atomic forces predicted by MLP.

Surface model	number of structures	$RMSE_E$ (meV)	$RMSE_F$ (meV/Å)
Step-free TiO_2(110)	613	1.766	103.5
TiO_2(110) with $[1\bar{1}1]$ step	664	1.139	112.9

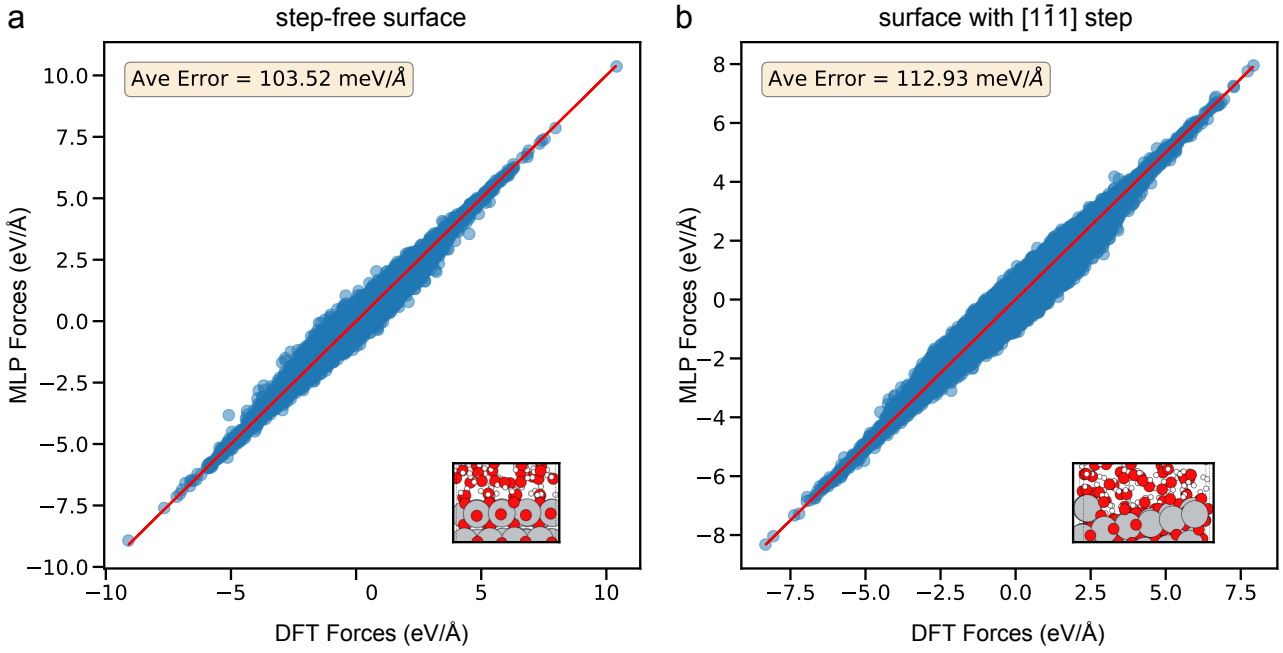

Figure S6. Comparison between atomic forces predicted by MLP and DFT calculation on (a) step-free rutile TiO_2 (110) water interface and (b) rutile TiO_2 (110) water interface with [1$\bar{1}$1] step.

Machine learning accelerated molecular dynamics

The machine learning potential adapted in this work is Deep Potential-Smooth Edition[8], and the training data were obtained by density functional theory calculation as implemented in the CP2K code.[9] The training data sets are generated with open-source deep potential generator package.[10] Details on training and validation of the machine learning potentials are given in the SI. The step-free rutile TiO_2 (110) surface was modelled by a symmetric periodic slab of five O-T-O tri-layers with a 8×4 supercell, and the size of the supercell is $23.67 \times 25.99 \times 38.53$ Å^3. For the surface with a $[1\bar{1}1]$ step, a 8×2 supercell was used with the exposure of the (9 10 1) surface, and the size is $27.02 \times 14.28 \times 48.15$ Å^3. The vacuum between the slabs is fully filled with water molecules, and as a result, the interface model of the step-free and stepped surface contain 2412 and 1785 atoms, respectively. The MLMD simulations were run by the LAMMPS package. NVT ensembles were imposed by the Nose-Hoover thermostat with the temperature of 330 K, and the MD time step was 0.5 fs.

MLMD and force prediction validation

To validate the accuracy of MLP, 100 configurations were randomly selected from the 20 ns MLMD trajectories of step models with terraces of 8 terminal Ti sites and 16 terminal Ti sites, and the corresponding atomic forces were computed with DFT. As can be seen in Figure S7, atomic forces predicted by MLP show good agreement with DFT validation. The RMSE values of atomic forces of different elements are shown in Table S3, indicating good accuracy in MLMD simulations.

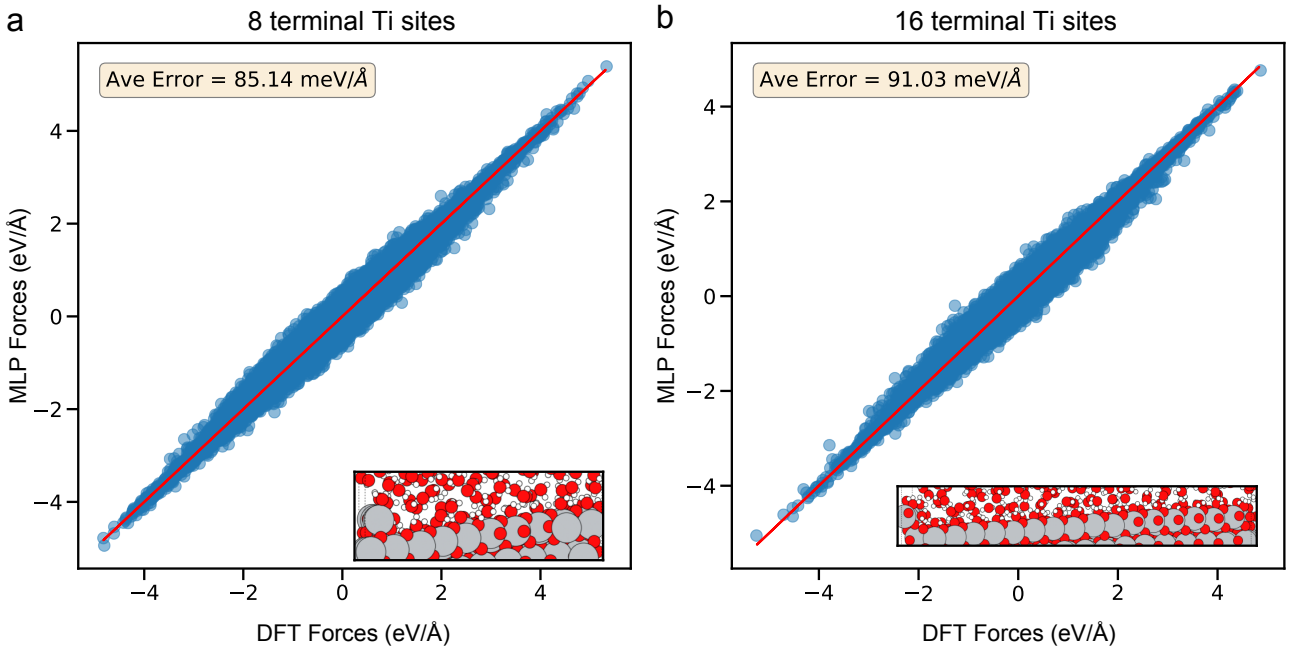

Figure S7. DFT validation for MLMD simulation of (a) 8 terminal Ti sites and (b) 16 terminal Ti sites model.

Table S3. RMSE of atomic forces ($RMSE_F$) of different elements and all atoms of MLP prediction are given for comparison. The unit for $RMSE_F$ is meV/Å

	$RMSE_F$(H)	$RMSE_F$(O)	$RMSE_F$(Ti)	$RMSE_F$
8-water step interface	90.9	82.4	71.1	85.1
16-water step interface	104.9	83.4	50.6	91.0

Density functional theory calculation

As shown in previous publication, Perdew-Burke-Ernzerhof (PBE) functional[11] with Grimme D3[12] dispersion correction shows similar description of interfacial structures as SCAN functional for TiO_2-water interfaces. [13, 14] For TiO_2-water interface under point of zero charge, PBE-D3 can already give accurate interfacial structures of TiO_2-water interfaces. Therefore, ab initio energies and forces for MLP training were calculated with the PBE-D3, as implemented in the freely available CP2K/QUICKSTEP package. [15] The core electrons were described by analytic Goedecker-Teter-Hutter (GTH) pseudopotentials. [16] The valence orbitals were represented in Gaussian-type double-ζ basis sets with one set of polarization function (DZVP) basis,[17] and an auxiliary plane wave basis with a cutoff of 800 Ry was used to re-expand the electron density in reciprocal space.[18] SCF convergence threshold was set to 1×10^{-6} a.u.[19, 20]

Water dissociation at TiO_2 water interface

Water dissociation at TiO_2 $(1\,1\,0)$ water interface is a long debating subject (see perspective [21]). Many people believe dissociation happens at surface vacancies, not perfect TiO_2 $(1\,1\,0)$ surface. [22, 23] Recently, molecular beam experiments by Wang *et al*. indicated water dissociation at non-vacancy sites is also possible. [24] The surface water dissociation process has been investigated systematically with MLMD in previous work.[25] In our MLMD simulations, we *did* notice surface water dissociation on rutile TiO_2 (110) surface with $[1\,\bar{1}\,1]$ step. We calculated the percentage of dissociated water, where water oxygen atoms with H coordination number less than 2 counted as dissociated water. The distance cutoff for calculation of H coordination number is 1.2 Å. Figure S8 shows the time accumulative average of degree of water dissociation for the last 2.5 ns of the 10 ns trajectories, indicating approximately 17% surface water dissociate for $[1\,\bar{1}\,1]$ stepped TiO_2 surfaces with 8 or 16 terminal Ti sites.

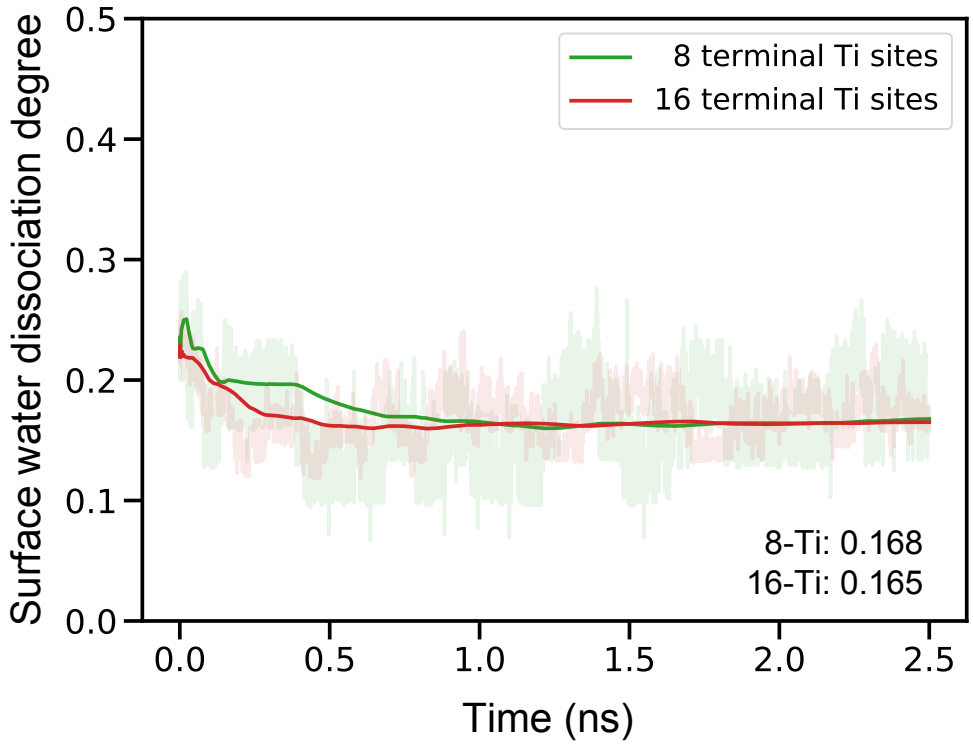

Figure S8. Time accumulative average of degree of surface water dissociation. Green and red colors represent results for our $[1\,\bar{1}\,1]$ stepped rutile TiO_2 (110) surface with 8 and 16 terminal Ti sites, respectively. Transparent shades are the instantaneous dissociation degree at every snapshot. Solid lines are time accumulative average of the dissociation degree.

Long-range effect

To validate the long-range effect of the atomic step from MLMD simulation, we expanded the width of terrace from 8 to 16 terminal Ti sites in the stepped surface model (from about 2.5 nm to 5 nm wide, see Table S1). Averaged distances between adsorbed water and its adjacent bridging oxygen on 16 terminal Ti surface are $d^{(l)}$ = 3.32 Å and $d^{(r)}$ = 3.18 Å, as shown in Figure S9. The characteristic of tilted surface water is consistent with that for the stepped surface with terrace of 8 terminal Ti sites, as presented in the main text. Based on the long range validation, we believe that this phenomenon can be expanded into a wider terrace on stepped surface, in good agreement with our EC-STM results.

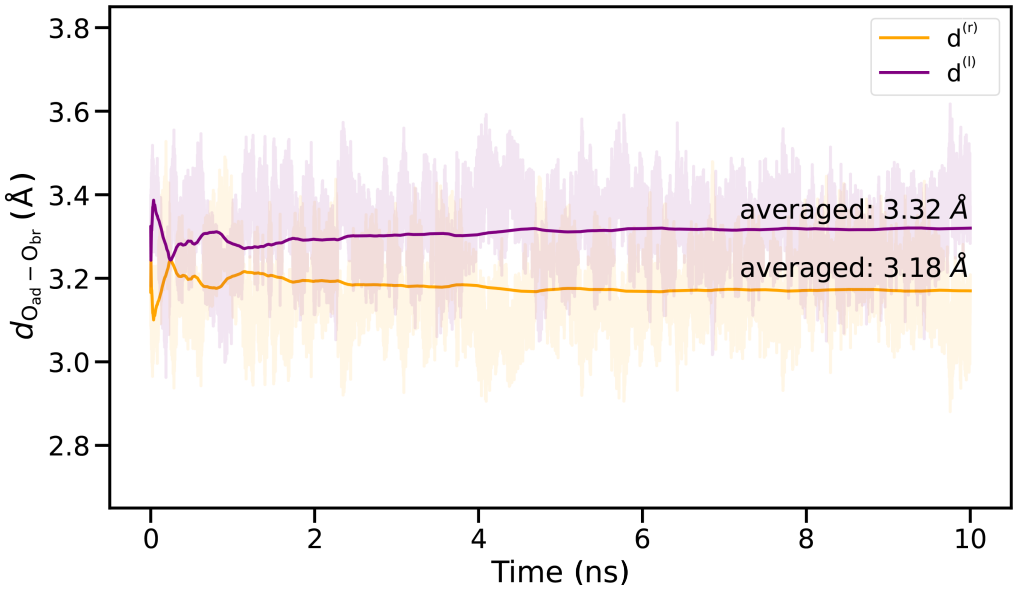

Figure S9. Horizontal distances between adsorbed water and the neighboring bridge O atoms in the step model with terrace of 16 terminal Ti sites from MLMD simulation.

TiO_2 surface with one layer of adsorbed water

When a step edge is introduced to the interface, H-bond network induced by the step edge would lead to shift of the O-O distances. To confirm this phenomenon, we perform the MLMD simulation of TiO_2-vacum interfaces with one monolayer of water adsorbed on TiO_2 surface. As shown in Figure S10, this model shows enhanced biased distances between adsorbed water molecules and bridge oxygen atoms, which means that the asymmetric distance is actually caused by the special geometry of steps. Furthermore, to validate the contribution of H-bond network, 3 adsorbed water molecules are removed from head and tail of the terrace so that the H-bond network along the terrace is broken. As shown in Figure S11, the asymmetric distances are absent with broken H-bond network. Therefore, the shift of adsorbed water is induced by step defect and propagate by H-bond network between adsorbed water.

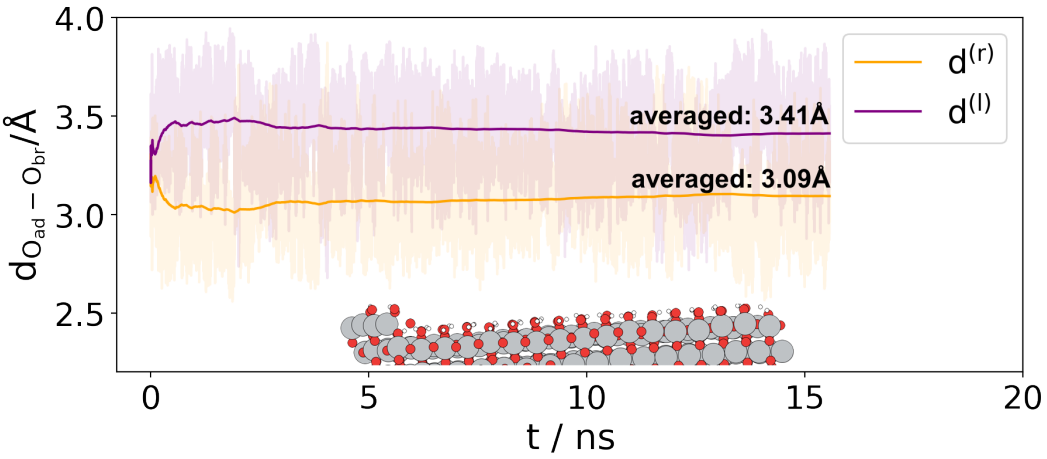

Figure S10. Horizontal distances between adsorbed water and the neighboring bridge O atoms in the step model with terrace of 16 terminal Ti sites with mono layer of water molecules from MLMD simulation. The structure is shown in the inset of the figure.

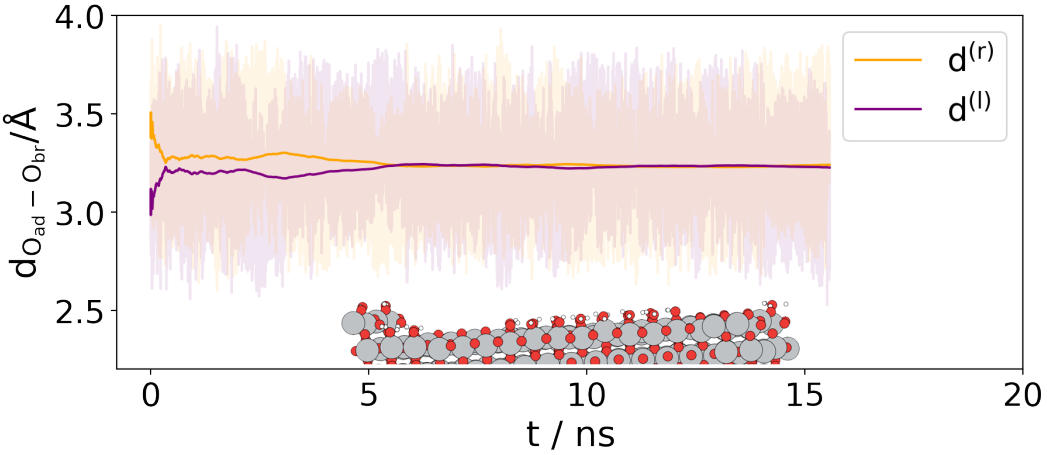

Figure S11. Horizontal distances between adsorbed water and the neighboring bridge O atoms in the step model with terrace of 16 terminal Ti sites with a mono layer of water molecule from MLMD simulation. To broke the H-bond network of the adsorbed water, 3 water molecules are removed from the head and tail of the terrace, respectively. The structure is shown in the inset of the figure.

XPS spectra of TiO_2 sample after EC-STM experiment

To rule out the dissolution of Pt from the Pt-Ir tip and its deposition on the TiO_2 sample surface during the EC-STM experiment, we performed XPS analysis on the TiO_2 sample used in the experiment. As shown in Figure S12, we obtained XPS spectra and Pt 4f spectra of the sample. The spectra clearly demonstrate the absence of Pt peaks, indicating that there was no Pt deposition on the TiO_2 surface during the EC-STM experiment.

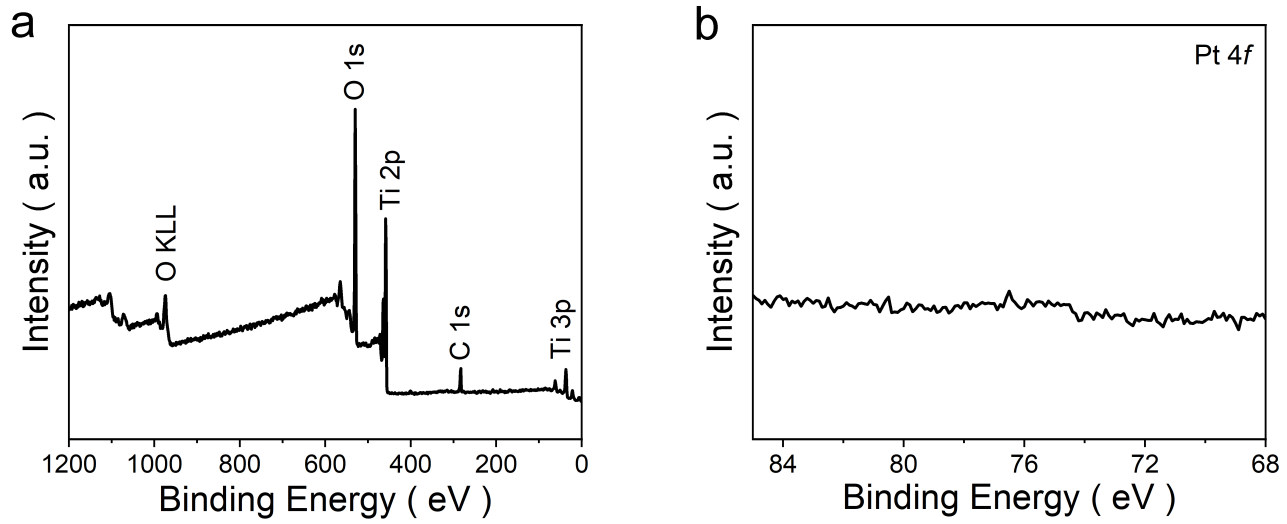

Figure S12. (a) XPS spectra of the TiO_2 (110) surface after EC-STM measurements. (b) Pt 4f spectra of the sample. XPS spectra confirms the absence of Pt deposition during the EC-STM.

Line profile of EC-STM image

To rule out that the new features are not due to the step edges, the corresponding line profiles of ES-STM images in Figure S4 and step in Figure 2c are provided in Figure S13c for comparison. As shown in Figure S13, the height of the double-row pattern varies from -60 pm to 80 pm, which is absolute different to the steps (from -200 to 200 pm).

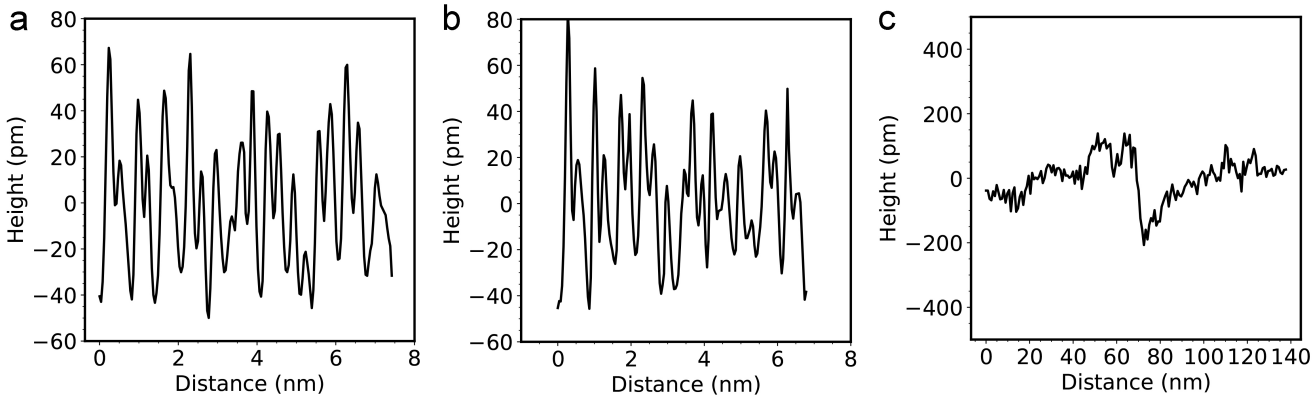

Figure S13. Line profile of EC-STM image in (a) Figure S4a and (b) Figure S4b. (c) Line profile of step in Figure 2c.

Fast Fourier Transform of STM

The points in white rectangle of FFT correspond to $[1\bar{1}0]$ periodicity of TiO_2 (110) in real-space image with 6.6 Å. This is consistent with the distance between double-row pattern.

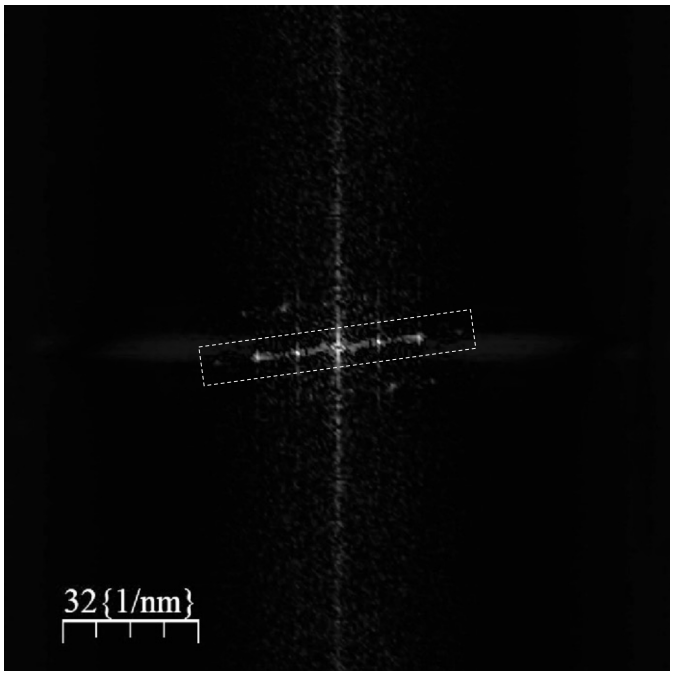

Figure S14. 2D fast Fourier transform (2D-FFT) of the STM image reported in Figure 2d.

Low-energy electron diffraction of rutile TiO_2 (110)

Based on the Low-energy electron diffraction (LEED) image in Figure S15, it is evident that the rutile TiO_2 (110) surface exhibits a (1×1) structure before being exposed to the electrolyte, which is consistent with the previous study.[26]

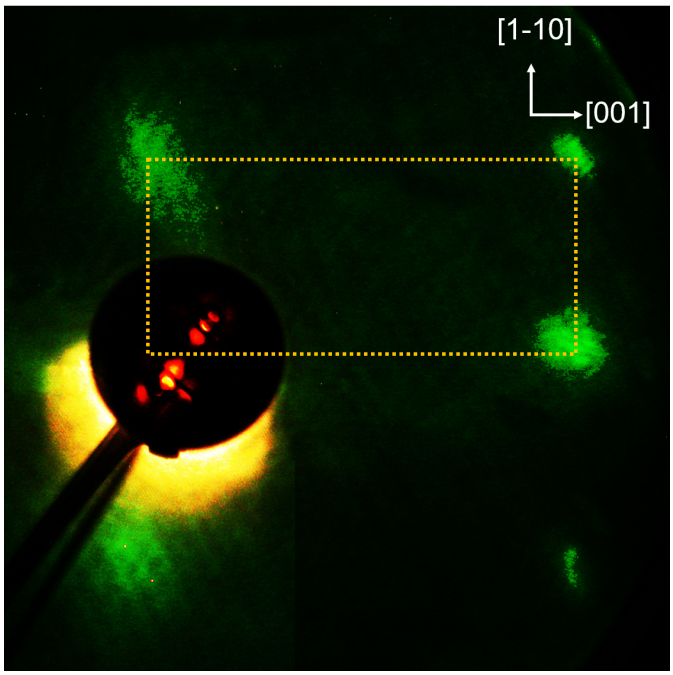

Figure S15. LEED pattern of the rutile TiO_2 (110) surface in UHV. The orange line highlights the rectangular (1×1) unit cell.

Crystallographic orientation determination

The commercially purchased rutile TiO_2 (110) single crystal has an edge with two chamfers, both of which are cut along the [001] direction. Thus, the direction of the chamfer edge is perpendicular to the [001] direction, as illustrated in the Figure S16a with the red marked edge indicating the beveled edge. Since the slow scan direction of the STM image in Figure 2c is along the [001] direction, the crystallographic orientation can be determined accordingly. Reflection high-energy electron diffraction (RHEED)[27, 28] pattern recorded from rutile TiO_2 (110) further confirms the crystallographic orientation. The electron beam is along the $[1\bar{1}0]$ direction.

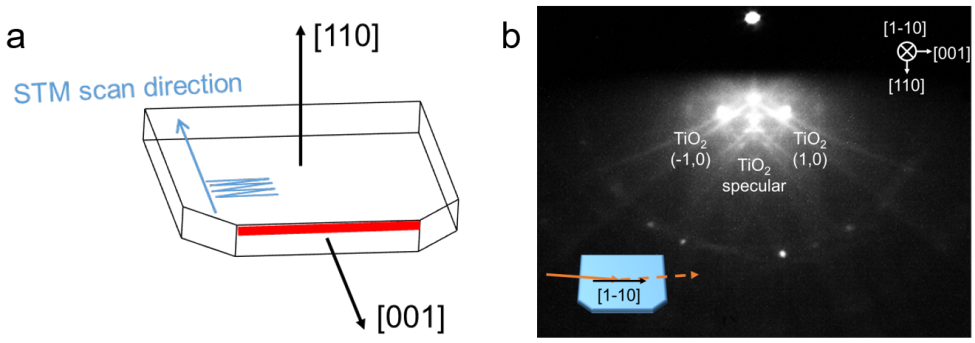

Figure S16. (a) The crystallographic orientation of rutile TiO_2 (110) single crystal purchased and illustration of STM scan direction. (b) RHEED pattern of rutile TiO_2 (110) in UHV with primary beam aligned along the $[1\bar{1}0]$ direction.

STM image in pH = 2 solution

Atomic resolved STM image in pH = 2 solution (0.01 M $HClO_4$) shown in Figure S17 exhibits same double-row pattern as the image in pH = 1.

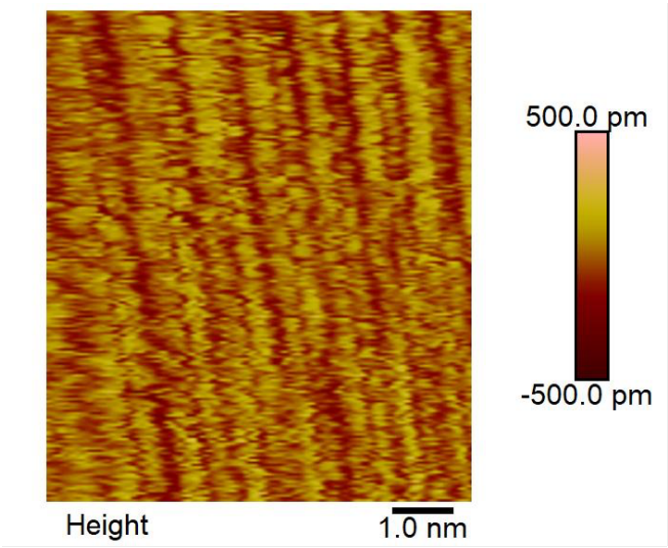

Figure S17. 7×8 nm^2 EC-STM image of the rutile TiO_2 (110) in 0.01 M $HClO_4$ (pH = 2) under E_{sample} = -0.45 V vs. SCE, E_{tip} = 1.27 V vs. SCE and I_{tunnel} = 1 nA.

References

1. Diebold, U. *et al.* Intrinsic defects on a TiO_2(110)(1×1) surface and their reaction with oxygen: a scanning tunneling microscopy study. *Surf. Sci.* **411**, 137–153 (1998).

2. Martinez, U., Vilhelmsen, L. B., Kristoffersen, H. H., Stausholm-Møller, J. & Hammer, B. Steps on rutile TiO_2(110): Active sites for water and methanol dissociation. *Phys. Rev. B* **84** (2011).

3. Hardcastle, T. P., Seabourne, C. R., Brydson, R. M. D., Livi, K. J. T. & Scott, A. J. Energy of step defects on the TiO_2 rutile (110) surface: an ab initio DFT methodology. *The J. Phys. Chem. C* **117**, 23766–23780 (2013).

4. Bandura, A. & Kubicki, J. Derivation of force field parameters for tio2- h2o systems from ab initio calculations. *The J. Phys. Chem. B* **107**, 11072–11081 (2003).

5. Zhang, L. *et al.* End-to-end symmetry preserving inter-atomic potential energy model for finite and extended systems. In Bengio, S. *et al.* (eds.) *Advances in Neural Information Processing Systems*, vol. 31 (Curran Associates, Inc., 2018).

6. Zhang, L., Lin, D.-Y., Wang, H., Car, R. & E, W. Active learning of uniformly accurate interatomic potentials for materials simulation. *Phys. Rev. Mater.* **3**, 023804 (2019).

7. Zhang, Y. *et al.* DP-GEN: a concurrent learning platform for the generation of reliable deep learning based potential energy models. *Comput. Phys. Commun.* **253**, 107206 (2020).

8. Wang, H., Zhang, L., Han, J. & E, W. DeePMD-kit: a deep learning package for many-body potential energy representation and molecular dynamics. *Comput. Phys. Commun.* **228**, 178–184 (2018).

9. VandeVondele, J. *et al.* Quickstep: fast and accurate density functional calculations using a mixed gaussian and plane waves approach. *Comput. Phys. Commun.* **167**, 103–128 (2005).

10. Zhang, Y. *et al.* DP – GEN: A concurrent learning platform for the generation of reliable deep learning based potential energy models. *Comput. Phys. Commun.* **253**, 107206 (2020).

11. Perdew, J. P., Burke, K. & Ernzerhof, M. Generalized gradient approximation made simple. *Phys. Rev. Lett.* **77**, 3865–3868 (1996).

12. Grimme, S., Antony, J., Ehrlich, S. & Krieg, H. A consistent and accurate ab initio parametrization of density functional dispersion correction (DFT-D) for the 94 elements H-Pu. *J. Chem. Phys.* **132**, 154104 (2010).

13. Wen, B., Calegari Andrade, M. F., Liu, L.-M. & Selloni, A. Water dissociation at the water–rutile tio2 (110) interface from ab initio-based deep neural network simulations. *Proc. Natl. Acad. Sci.* **120**, e2212250120 (2023).

14. Zhuang, Y.-B., Bi, R.-H. & Cheng, J. Resolving the odd–even oscillation of water dissociation at rutile tio2 (110)–water interface by machine learning accelerated molecular dynamics. *The J. Chem. Phys.* **157** (2022).

15. Kühne, T. D. *et al.* CP2K: An electronic structure and molecular dynamics software package - quickstep: efficient and accurate electronic structure calculations. *J. Chem. Phys.* **152**, 194103 (2020).

16. Goedecker, S., Teter, M. & Hutter, J. Separable dual-space gaussian pseudopotentials. *Phys. Rev. B* **54**, 1703–1710 (1996).

17. VandeVondele, J. & Hutter, J. Gaussian basis sets for accurate calculations on molecular systems in gas and condensed phases. *J. Chem. Phys.* **127**, 114105 (2007).

18. Lippert, G., Hutter, J. & Parrinello, M. A hybrid gaussian and plane wave density functional scheme. *Mol. Phys.* **92**, 477–487 (1997).

19. Hamilton, T. P. & Pulay, P. Direct inversion in the iterative subspace (DIIS) optimization of open-shell, excited-state, and small multiconfiguration SCF wave functions. *J. Chem. Phys.* **84**, 5728–5734 (1986).

20. VandeVondele, J. & Hutter, J. An efficient orbital transformation method for electronic structure calculations. *J. Chem. Phys.* **118**, 4365–4369 (2003).

21. Diebold, U. Perspective: A controversial benchmark system for water-oxide interfaces: H2o/TiO2(110). *The J. Chem. Phys.* **147**, 040901 (2017).

22. Wendt, S. *et al.* Formation and splitting of paired hydroxyl groups on reduced TiO_2 (110). *Phys. review letters* **96**, 066107 (2006).

23. Liu, L.-M., Zhang, C., Thornton, G. & Michaelides, A. Structure and dynamics of liquid water on rutile $tio_2(110)$. *Phys. Rev. B* **82**, 161415 (2010).

24. Wang, Z.-T. *et al.* Probing equilibrium of molecular and deprotonated water on TiO2(110). *Proc. Natl. Acad. Sci.* **114**, 1801–1805 (2017).

25. Zhuang, Y., Bi, R.-H. & Cheng, J. Resolving the odd-even oscillation of water dissociation at rutile TiO_2(110)-water interface by machine learning accelerated molecular dynamics. *J. Chem. Phys.* (2022).

26. Serrano, G. *et al.* Molecular ordering at the interface between liquid water and rutile TiO_2 (110). *Adv. Mater. Interfaces* **2**, 1500246 (2015).

27. Gao, Y. & Chambers, S. A. Effect of substrate orientation on the crystal quality and surface roughness of nb-doped tio2 epitaxial films on tio2. *J. materials research* **11**, 1025–1029 (1996).

28. Chen, X., Gao, W., Sivaramakrishnan, S., Hu, H. & Zuo, J. In situ rheed study of epitaxial gold nanocrystals on tio2 (1 1 0) surfaces. *Appl. surface science* **270**, 661–666 (2013).